Measurement and Tracking of Blowing and Falling Snow Particles Using an Automotive 1550 nm LiDAR

Nikolas Aksamit[a], Masaki Nemoto[b], Yoichi Ito[c]

[a]*Institute for Mathematics and Statistics, UiT - The Arctic University of Norway, , Tromsø, 9037, Norway*
[b]*Shinjo Cryospheric Environment Laboratory, National Research Institute for Earth Science and Disaster Resilience (NIED), Shinjo, 9960091, Japan*
[c]*Snow and Ice Research Center, National Research Institute for Earth Science and Disaster Resilience (NIED), Nagaoka, 9400821, Japan*

Abstract

The prevalence and affordability of fast-scanning commercially available LiDARs are increasing due to the rapid expansion of the autonomous vehicle industry. These LiDAR units can provide >1 Hz measurements of millions of laser reflections at ranges of hundreds of meters with high precision. In this study we investigate the often overlooked 1550 nm wavelength LiDAR for measurements of airborne blowing and falling snow particles. While reflectance of snow is known to be lower at 1550 nm than shorter wavelengths, the reduced sensitivity of the human eye to this wavelength allows these LiDARs to be produced with much greater laser power, lower beam divergence, and longer range. As exact laser specifications are rarely published due to commercial interests, there is limited potential for estimating the performance of new fast-scanning LiDAR theoretically. In lieu of this, we performed an initial systematic analysis of a 1550 nm LiDAR in controlled blowing and falling snow experiments at the Cryospheric Environment Simulator. We find that commercially available 1550 nm LiDAR can indeed provide reliable high spatiotemporal resolution measurements of volumes of both blowing and falling snow. Furthermore, we find that large falling precipitation particles (>1 mm) can be tracked at distances of up to 10 meters away for several seconds. The future implementation of such an instrument in field studies can provide new insights into our understanding of the critical spatial and temporal heterogeneity of turbulent wind-snow processes.

Keywords: blowing snow, drifting snow, snowfall, LiDAR, particle tracking

1. Introduction

Accurate measurements of blowing and falling snow rates are critical for predicting cold-region snow mass balances, surface–atmosphere exchanges, and visibility reduction. Wind-driven snow transport (e.g., blowing snow and preferential deposition) is also responsible for time-varying accumulation patterns, significant basin-scale sublimation losses of water, and increased avalanche hazard. The exact coupling of natural wind and snow remains difficult to predict due to strong spatial and temporal variability caused by millimeter scale particle dynamics in complex turbulent flows composed of large scale coherent structures (Aksamit and Pomeroy, 2017; Nishimura et al., 2024). Obtaining high spatiotemporal resolution measurements (mm and sub-second scale) over large atmospheric volumes (hundreds of m^3) of airborne snow would help resolve open questions that cannot be answered with fixed-point measurements of blowing and falling snow, such as snow particle counters and laser disdrometers (Löffler-Mang and Joss, 2000; Kinar and Pomeroy, 2015). Specifically, such large volume data would allow users to quantify the natural spatial heterogeneity in airborne snow concentrations that is caused by atmospheric turbulence and coherent structures and governs transport.

Sub-second and cm-resolution large volume measurements of falling snow velocity and concentration in natural settings have been achieved with multi-camera particle tracking systems. These systems, however, require specialized experimental fluid dynamics software, a large number of synchronized cameras to obtain reliable three-dimensional positions of small particles, and significant external lighting sources (see, e.g., Toloui et al., 2014; Li et al., 2021, 2024; Muller, 2025). As such, broad applications of these tools is unlikely, especially at remote meteorological observation sites with limited infrastructure. More widely used ground and remote sensing based systems also exist for measuring airborne frozen precipitation and blowing snow over large regions, though the data is not available at the necessary spatial or temporal scales to resolve near-surface turbulent wind-snow coupling (Tapiador et al., 2012; Gossart et al., 2017; Palm et al., 2017).

Aircraft and terrestrial LiDAR systems have emerged as reliable tools to obtain mm-accurate measurements of snow-covered surfaces over large regions (Prokop, 2008; Deems et al., 2013). LiDAR systems most prominently used in snow and cryospheric studies operate at wavelengths in the visible or near-infrared (NIR), particularly near 532 nm and 1064 nm. These wavelengths are favored because clean, dry surface snow exhibits relatively high reflectance (60-90%) and produces strong backscatter signals. In contrast, the 1550 nm wavelength has a surface snow reflectance typically of less than 10% (Warren, 2019). Aircraft and terrestrial LiDAR at 1064

nm, in particular, have been widely adopted for snow depth mapping due to its balance between sufficient reflectance and limited penetration into the snowpack, yielding reliable surface returns (Deems et al., 2013). These landscape scans occur on the order of minutes or hours, timescales much longer than that of the surface turbulence. The signal interception by blowing and falling snow particles is treated as a source of detrimental noise that must be filtered effectively (Clemens-sewall et al., 2022). The question then arises, can researchers extract this airborne particle signal in higher temporal resolution LiDAR scans for meaningful coupled wind-snow studies?

In recent years, the rapid expansion of the autonomous vehicle industry has buoyed significant advances in commercially available fast-scanning and high-resolution LiDAR systems, primarily in the 905 and 1550 nm wavelengths (Dai et al., 2021); the former due to lower cost silicon sensors and latter due to their enhanced eye-safe nature. This growth industry has generated both increases in unit capabilities and significant decreases in unit price. Recently, a low-cost 905 nm LiDAR was successfully tested for measurement of snow surface changes (Ruttner et al., 2025), but to date no conclusive study has been performed for evaluating measurements of airborne snow particles with any fast-scanning instruments for cryospheric science purposes.

Due to the accelerating pace of the autonomous vehicles industry and its reliance on fast-scanning LiDARs for navigation, understanding the interference of airborne frozen precipitation on LiDAR measurements is an active field of research. A range of studies, both theoretical and experimental, have worked to better understand the degree to which LiDAR scans of background surfaces are obstructed by blowing and falling snow (see, e.g., Wojtanowski et al., 2014; Jokela et al., 2019a,b; Kutila et al., 2020; Hahner et al., 2022; Teufel et al., 2022; Sun et al., 2024). These experiments have been performed in a number of regions across the globe, with different LiDAR units, and in different weather conditions. Due to the significant interference caused by airborne snow backscatter, considerable effort has also been expended in developing algorithms to efficiently remove the presence of snow particles in automotive LiDAR navigation scans (e.g., Wang et al., 2022). A familiar rationale exists in the field of autonomous driving that suggests the low reflectance at 1550 nm would generate a higher signal-to-noise ratio for observing objects obscured by the airborne snow (i.e., less snowy data). Perhaps because of this, the primary focus of experimental studies on snow signal interference in automotive LiDARs has focused on wavelengths below 1000 nm. As such, there is limited experimental validation of airborne snow backscatter rates with 1550 nm automotive LiDAR.

The notable exception to this pattern is the direct experimental comparison of 1550 and 905 nm automotive LiDARs during active snow storms by Mattson et al. (2025). They found that their 1550 nm LiDAR actually obtained a greater percentage of airborne snow returns, as well as snow returns at greater distance than their 905 nm unit. In high-wind snowfall conditions, their 1550 nm LiDAR returns consisted of between 40% and 90% airborne snow. The 905 nm LiDAR scans consisted of between 0-70% airborne snow, with higher percentages of airborne snow signal occurring most frequently with the 1550 nm LiDAR unit across a range of conditions.

While this appears counterintuitive when focused solely on signal reflectance, the measured backscatter signal is also a function of the power of the transmitted laser and the sensitivity of the photodetector. For civil automotive applications, laser power is governed by the maximum permissible exposure of light, in units of energy per area, that is considered safe. Below 1400 nm, light can cause greater damage to the retina, and thus laser power is limited. Because of this, 1550 nm LiDARs are permitted to operate with much higher laser power and are becoming a popular choice for some automakers due to their increased range and performance and reduced beam divergence (e.g., greater accuracy) (Mattson et al., 2025). Indeed a high-power 1550 nm laser can generate orders of magnitude more photons than lower wavelength LiDARs while staying within eye-safe ranges. The low beam divergence may also enhance the identification of small airborne particles. Thus, higher allowable peak and average power can directly increase the received signal strength and improve signal-to-noise ratios, particularly for weakly reflecting targets or measurements dominated by volumetric backscatter (e.g., blowing snow clouds).

One other potential advantage of 1550 nm LiDAR for those interested in detecting airborne snow is their use of InGaAs photodetectors and a potentially clearer backscatter signal. InGaAs photodetectors are a historically more expensive and less mature technology than the silicon-based detection used at lower wavelengths, however this cost gap is quickly closing. InGaAs detection at 1550 nm is less susceptible to noise from background solar sources, resulting in a lower noise floor than eye-safe 905 nm LiDAR. Light at 1550 nm also has very low penetration in snow (Deems et al., 2013). All this implies that, if the power of the laser is high enough to get a return, the particle position can be very accurate. These combined effects may explain the experimental findings of enhanced airborne snow signals at 1550 nm from Mattson et al. (2025).

In our study, we investigate the ability of a commercially available 1550 nm LiDAR to obtain measurements of blowing and falling snow in volumes of air on the order of 10-150 m^3 at sub-second and mm resolutions. Specifically, we are interested in whether these airborne snow backscatter signals under blowing and falling snow conditions can provide spatiotemporal proxies that are meaningful for cryospheric, meteorological, or hydrological science applications. These studies were performed with maximum control in the Cryospheric Environment Simulator at the Shinjo Branch of the National Research Institute for Earth Science and Disaster Resilience, Japan. We evaluated the LiDAR performance for a range of wind speeds and snowfall rates in a cold room laboratory environment relative to a high resolution snow particle counter and rapid-response snow accumulation scale. Our experimental study provides an informative counterpoint to the common narrative against using 1550 nm LiDAR for snow studies. By demonstrating the feasibility and limitations of a low-cost 1550 nm LiDAR for snow particle detection, this work

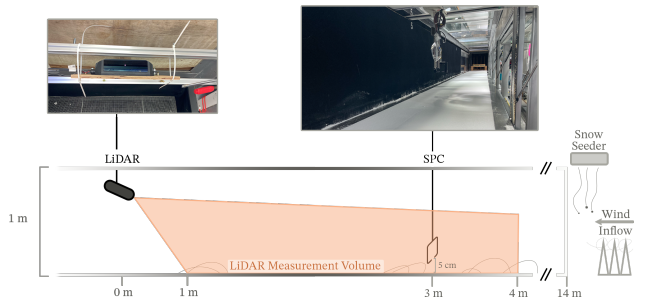

Figure 1: Schematic of wind tunnel blowing snow experiment with photographs of relative LiDAR and SPC positioning.

explores the potential for repurposing increasingly accessible and cost effective high-power automotive LiDAR systems as new tools for cryospheric research.

2. Methods

2.1. Laboratory Facility

We performed blowing and falling snow experiments at the Cryospheric Environment Simulator (Abe and Kosugi, 2019), Shinjo Branch of the National Research Institute for Earth Science and Disaster Resilience (NIED), Japan in July, 2025. These experiments were designed to evaluate the efficacy of a commercially available, fast-scanning (10 FPS), high-resolution (>1 million pts/s) LiDAR in obtaining meaningful measurements, or measurement proxies, of blowing and falling snow. Both blowing and falling snow experiments were conducted inside the cold room, which was kept at a near constant $-10°C \pm 0.5°C$.

Wind-snow couplings in blowing and falling snow are closely linked processes, but, in nature, particle sizes and wind velocity can vary widely between them. We mimic these differences in our experiments using small sieved snow particles for the blowing snow experiments that represent heavily fractured grains and fresh dendritic and aggregate grains grown in the snowfall simulator for the falling snow experiments.

We used the 14 m × 1 m × 1 m cold room wind tunnel at variable wind speeds for our blowing snow experiments (Fig. 1). Large-scale vortices are generated with fixed spires on the upstream inlet of the wind tunnel, creating a logarithmic profile in the observation section (Nemoto et al., 2014). Snow grains for the blowing snow wind tunnel were "Type B" ice particles obtained from the snowfall generator and stored at -15°C (Abe and Kosugi, 2019). Prior to each experiment, the bottom of the wind tunnel was filled with an approximately 2 cm thick bed of sieved snow crystals. Snow was sieved and uniformly smoothed along the wind tunnel bed to allow for active splash and entrainment along the entire length of the observations. Three experiments were performed at inlet wind speeds of 8, 10, and 12 m/s. Each experiment lasted for sixty seconds once the desired free-stream velocity was achieved.

The LiDAR was installed on the inside ceiling of the wind tunnel at the downwind end, obtaining usable surface

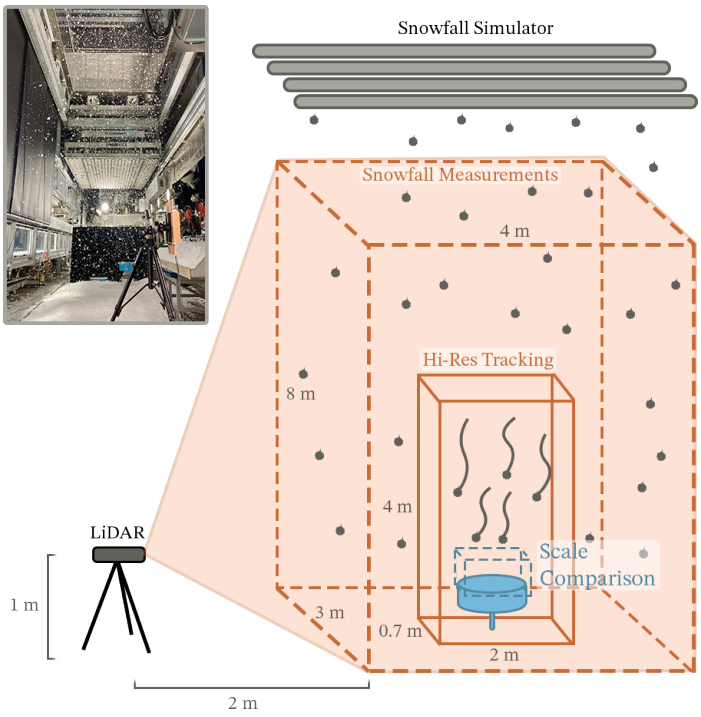

Figure 2: Photograph and schematic of snowfall simulator particle tracking experiment.

measurements spanning approximately 4 meters of the wind tunnel (Fig. 1). We angled the LiDAR at 24 degree downwards to get measurements of the bed surface more than one meter away from the LiDAR unit (Figure 1). A snow particle counter (SPC) was positioned approximately three meters upwind in front of the LiDAR, five centimeters above the snow surface. LiDAR returns from the SPC and the shadow it created in the wind tunnel were removed from the subsequent analysis.

For the snowfall experiments, "Type A" dendritic snow crystals were grown on the third floor of the Cryospheric Environment Simulator and provided a finely controlled simulation for our LiDAR snowfall detection tests (Abe and Kosugi, 2019). Snow is grown on a roller of wire mesh in a process comparable to atmospheric dendrite growth. The dendrites are then removed by a piano wire as the roller rotates against it. This gradually releases the snow, with the snowfall rate being controlled by the speed of rotation. The low turbulence environment during growth and the scraping process facilitate large crystal growth and aggregation (see, e.g., Figure 3). The larger crystals are easily followed between LiDAR scan lines which enabled particle tracking and velocity measurements, as described in Section 3.

The third floor snowfall simulator creates a unique 3 m × 5 m snow fall footprint in the middle of the cold room. Due to dispersion of the falling particles, we performed LiDAR analysis in a slightly larger 3 m × 6 m × 8 m volume of snowfall from outside the precipitation region (orange dashed lines, Fig. 2). In the interior of the full volume we performed particle tracking in a smaller high-resolution region with greater scan line density (orange solid lines, Fig. 2).

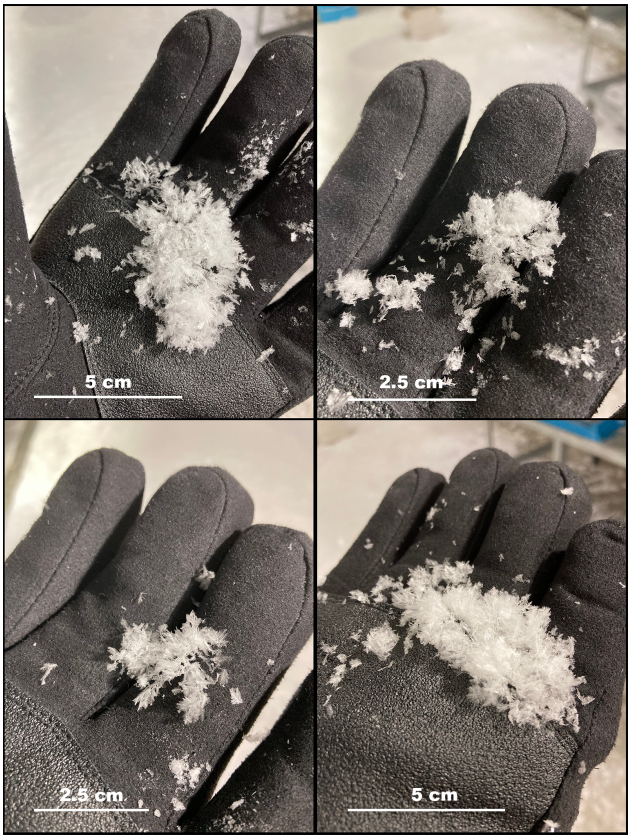

Figure 3: Four samples of "Type A" aggregate grains and individual dendrites from the snowfall simulator. These particles landed on the gloved hand while falling from the ceiling of the Cryospheric Environment Simulator with the photographs taken immediately afterward. The photos show typical “large grains” whose trajectories could be tracked in LiDAR data. An approximate scale is added for each photograph.

We also collected concurrent measurements of snowfall accumulation with a high-resolution high-frequency snow scale mounted with a circular 60-centimeter diameter collection bucket located approximately 6 meters away from the LiDAR (blue bucket, Fig. 2). Using the cross-sectional area of the collection bucket on top of the scale, we were able to process the data and obtain 1 Hz measurements of effective snowfall rate in units of mm/hr of snow water equivalent (SWE). Immediately above this scale we conducted a focused particle counting corresponding with particles that contribute to these 1 Hz measurements (blue dashed box). These analyses are further decribed in Section 3. Snowfall was generated for four hours with snowfall rates varying from <0.25 mm snow water equivalent per hour, to greater than 6 mm snow water equivalent per hour when the apparatus was being cleaned. During this four-hour period, we conducted seventeen 60-second LiDAR observations.

2.2. Instrumentation

The LiDAR under investigation is the automotive-grade 1550 nm Seyond Falcon K1 (Fig. 1). Instrument specifications can be found in Table 1. Notably, this LiDAR can measure 1.25 million points per second at 10 frames per second. It has a user-adjustable central high-resolution region of interest with $0.05^\circ \times 0.05^\circ$ angular resolution embedded in a larger field of view with $0.1^\circ \times 0.1^\circ$ angular resolution. The reported range of this LiDAR is 500 m, with a beam divergence of less than 0.1°, suggesting a high energy output that may compensate for lower reflectivity of snow at this wavelength. The LiDAR contains one detector and is susceptible to shadowing caused by the first reflection in the line of sight. It is, however, possible to configure with multiple synchronized units to avoid shadowing.

Blowing snow flux comparisons were performed against a Snow Particle Counter (Niigata Denki Co.) (Sato et al., 1993) mounted at a fixed height of 5 cm in the mid-section of the wind tunnel during all experiments (Fig. 1). Both blowing snow fluxes and particle counts for discrete diameter bin ranges were recorded with 1 Hz sampling. Snowfall measurements were verified by a high-precision high-frequency scale situated in the center of the snowfall area. These instruments allowed second-scale verification of blowing and falling snow fluxes measured by the LiDAR.

Table 1: Seyond Falcon K1 Instrument Configuration

Wavelength	1550 nm
Range	1 - 500 m
Detection Range	500 m (250 m @ 10% Reflectivity)
Vertical Scanning Lines	150 lines, 1480 lines/sec
Inner FOV	$120^\circ \times 9.6^\circ$ (Configurable)
Angular Resolution	$0.051^\circ \times 0.053^\circ$ (Configurable)
Points per second	1.25 Million
Frame Rate	10 FPS
Beam Divergence	$< 0.1^\circ$
Laser Safety	Class 1
Operating Temperature	-40°C - 80°C

3. Results

Blowing and falling snow experiments were conducted in the cold room at the NIED Cryospheric Environment Simulator in July 2025 to test the efficacy of a commercially available 1550 nm LiDAR for measurements of airborne snow in a variety of conditions. Our results suggest that for both blowing and falling snow, the LiDAR has promising capabilities for measuring proxies of surface blowing snow fluxes and snowfall rates. Additionally, the LiDAR can capture nonstationary spatiotemporal structures (e.g., snow waves, snow snakes/streamers, wakes) in surface blowing snow that are not directly resolvable from point measurements (see, e.g., Nishimura et al., 2024). We find, for suitably large falling snow particles, particle tracking is also possible, providing a potential alternative to cumbersome outdoor camera-based particle tracking velocimetry (PTV) systems.

3.1. Blowing Snow Detection

We conducted three identical experiments in the blowing snow wind tunnel with variations in prescribed wind speed: 8 m/s, 10 m/s, and 12 m/s. Mean wind speed and turbulence intensity as measured at 12 cm above the snow surface for the three freestream velocities can be found in Table 2. We calculated the friction velocity from a best-fit log-profile to wind speeds measured at six heights, from four to twenty centimeters. Wind tunnel statistics were calculated during identical blowing snow experiments immediately following the LiDAR tests to avoid further obstructing the flow or LiDAR view.

Table 2: Wind Tunnel Experiment Statistics: Mean wind speed ($\overline{U}$) and turbulence intensity (TI) are calculated for with a sonic anemometer at 12 cm height. Friction velocity (u_*) is calculated with a best-fit log-profile from six measurement heights in the lowest 20 cm.

Experiment	$\overline{U}$ (m s^{-1})	u_* (m s^{-1})	TI (-)
8 m/s	5.739	0.306	0.113
10 m/s	7.162	0.365	0.135
12 m/s	8.555	0.429	0.161

The blowing snow consisted of fine-grained particles, with more than half of the particles having a diameter smaller than 100 μm. The probability distribution of snow particle diameters spanning all experiments follow a common gamma distribution, shown in Figure 4. Obtaining a LiDAR return from these saltation clouds at distances of two to six meters likely relies on volumetric backscatter from a collection of fine ice crystals instead of individual particle returns. This is a slightly different measurement process than for large snow particles, and may actually result in greater reflectance at the 1550 nm wavelength than the often quoted <10% (Warren, 2019).

The wind tunnel LiDAR measurements provide point-clouds of both surface and airborne particles during the experiments. Using surface scans immediately prior to the onset of blowing snow as a background reference, our initial analysis simply involved counting LiDAR returns greater than three centimeters above the bed. This minimum height is slightly lower than the height of the SPC, but allowed for some measurement uncertainty at the far end of the wind tunnel. Concurrently, the SPC provided snow particle counts and mass flux at one second intervals. Given the wind speed magnitudes and length of the observation section, one-second SPC recording intervals correspond with potential flux of all airborne particles out of the four square meter LiDAR measurement window. For this reason, our initial investigation compares one second averages of airborne particles from individual LiDAR frames with concurrent SPC flux (Figure 4b). All three experiments follow a similar nearly linear shape, suggesting a relatively consistent functional relationship exists between the LiDAR signal and SPC measurements. The most consistent outlying values occur during the 8 m/s experiment, during which saltation clouds only intermittently pass the SPC at its 5 cm height. We investigate this LiDAR-flux connection more closely in Figure 5 where time series of both signals are compared.

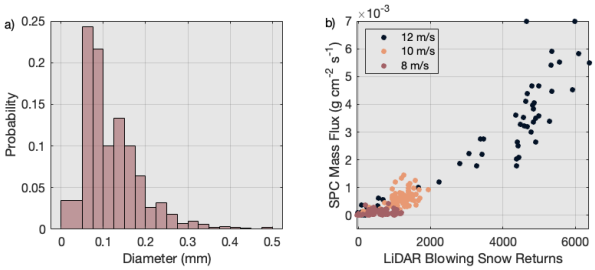

Figure 4: Probability distribution of "Type B" snow particles measured by SPC over all wind tunnel experiments. Nonlinear relationship between 1 Hz LiDAR particle counts above 3 cm height and SPC mass flux.

Figure 5 details the full temporal evolution of blowing snow transport for each experiment at the SPC in red. Thin black curves show 10 Hz LiDAR counts, with thick black curves detailing a 1 Hz moving-average. Snow accumulated in the downwind region of the wind tunnel in all experiments, but the precise height of time-varying surface changes was largely obscured in the LiDAR data by the saltation clouds. To account for this, we perform a linear detrending on the time series of LiDAR particle counts to account for deposition changes from the pre-transport surface. During the 8 m/s experiment (Fig. 5a), the SPC measured a low average mass flux with large fluctuations only occurring as intermittent waves of particles passed the five centimeter high instrument. In contrast, the LiDAR obtained a smoother signal of transport with the onset and conclusion of transport coinciding perfectly between devices.

As we increased the wind speed, the mass flux became more consistent in the SPC signal, and strong temporal coherence of individual flux spikes appeared between the LiDAR and SPC signals. For example, in 10 m/s winds (Fig. 5b) the transport durations again match, and there is also a correlation between three distinct mass flux oscillations occurring with an approximate twenty second period peaking at 30 seconds, 50 seconds, and 80 seconds. Between these low frequency peaks, further correspondence between even shorter scale transport phenomena are evident on 1 to 3 second time scales.

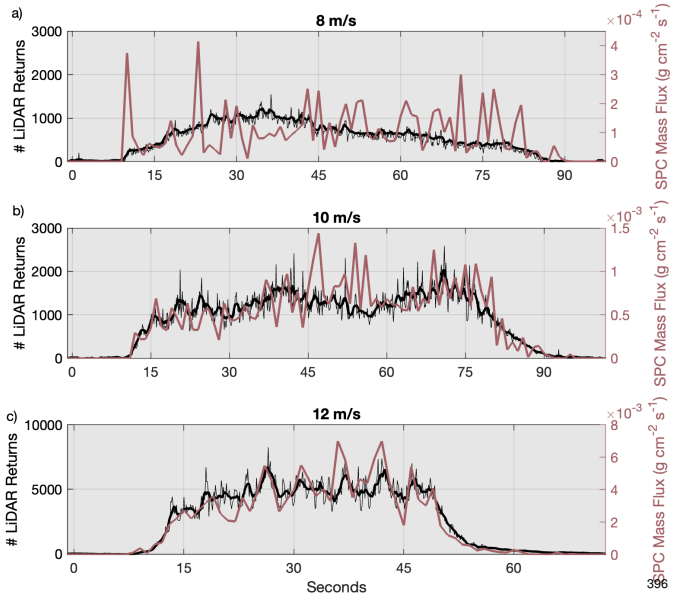

Figure 5: Comparison of LiDAR-derived blowing snow cloud returns and Snow Particle Counter Mass Flux for three wind tunnel experiments. Note the order of magnitude differences in values for both LiDAR counts and SPC mass flux across the three wind speeds.

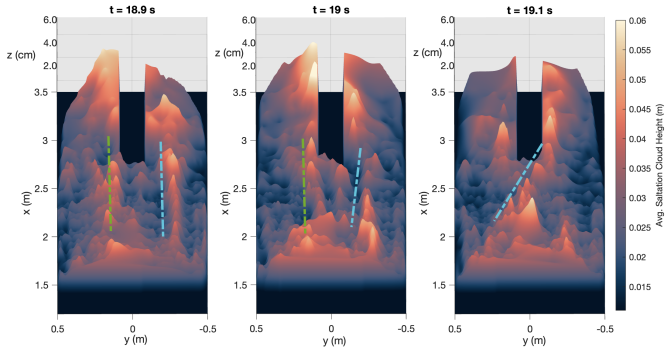

Figure 6: Sequential frames of blowing snow surface structures (snow snakes) in the NIED wind tunnel. Features at a greater distance appear larger due to the low angle line-of-sight and greater return spacing. For a full animation, see the Supplementary Material.

At 12 m/s, we find the strongest connection between intermittent snow transport fluctuations in both instruments. Figure 5c shows every spike in SPC flux is matched by a spike in the 1 Hz LiDAR signal. This suggests a strong capacity of 1550 nm LiDARs to record meaningful high temporal resolution bulk saltation measurements. SPC flux values oscillate up to $4{\times}10^{-3}$ g cm^{-2} s^{-1} during transport, which is more than double the max transport at 10 m/s. This suggests strong intermittency and the passage of coherent waves of saltation. We can also resolve these spatially coherent features in the LiDAR data, as well as their transient temporal evolution.

To visually investigate such features, we first process the LiDAR point clouds by removing spurious returns far from the densest clouds. To do this, we calculate the median distance of each point to its 10 nearest neighboring points (hereafter referred to as $\overline{NN}_{10}$). This provides a distribution of particle concentrations, from which we remove all points with greater than 92nd percentile of sparsity. What remains are LiDAR particles returns in the densest region of the flow, which we can then interpolate to a gridded surface. We use a Gaussian filter on this surface of interpolated clouds with a standard deviation smaller than experiment-averaged $\overline{NN}_{10}$, to get a clear visualization of saltation cloud heights (Fig. 6).

In Figure 6 we show an example of the morphology of two streamwise features (i.e., snow snakes/streamers) that extend the down the wind tunnel on either side of the SPC (central data gap) during the 12 m/s experiment. The green and blue lines highlight the approximate linear apex of these saltation features, initially contouring the outside of the wake caused by the SPC in the first frame. These features then begin to merge behind the SPC in Frame 2, with only a single linear feature remaining in the wake in Frame 3. The snow snakes evolve at sub-second timescales because they are generated by turbulent wake structures organizing the blowing snow particles. At these timescales, it is highly unlikely that surface roughness effects could result in these migrating snow-snake-shaped surface transport distributions. A complete animation of the 12 m/s saltation surface is available in the Supplementary Material. This video shows the empty wind tunnel, onset of transport, evolution of surface streamers, and cessation of transport.

Such qualitative spatiotemporal structures also have a quantifiable impact on both the LiDAR point clouds and total blowing snow flux. In addition to snow snakes, migrating lateral bands of snow (e.g., snow waves) appear as persistent features throughout the data. To quantify the advection of these passing waves, we divided the measurement domain into three 20-cm long regions, spanning the width of the wind tunnel, perpendicular to the flow. We then regenerated LiDAR particle count time series for each region in the highly turbulent 12 m/s experiment. We further calculated the cross-correlation between each time series and identified the time lag of maximum correlation. This effectively tracked the passage of local flux maxima in the 10 Hz LiDAR signal down a 2.5 meter section of the wind tunnel. In Table 3, we label each region by its upstream distance from the LiDAR, with the wind flowing towards the LiDAR. The time lags of maximum correlation between each region show the snow wave transit times are only slightly slower than the wind speed (~7-10 m/s), but consistent between all three regions. This provides further evidence we are able to actually track physical waves of saltation as they migrate along the snow surface in the wind.

It is worth noting that blowing snow measurements were also attempted in a spanwise orientation with the LiDAR outside the wind tunnel. Unfortunately, the glass diminished the laser signal to a significant degree. No meaningful snow measurements were retrievable from those experiments, though such measurements might be possible with an even higher powered laser or specialized viewing windows.

Table 3: Time lag of maximum correlation, and correlation coefficient, for regional 10 Hz particle count time series. Airborne particles are counted in tunnel-wide 20 cm long bands centered at the marked distances. Distances are measured from from the LiDAR with distance decreasing in the direction of the flow. Positive time lags indicate structures migrating downwind.

Regions	4 m	3 m	2 m
3 m	0.1 s, r=0.76		
2 m	0.3 s, r=0.63	0.1 s, r=0.70	
1.5 m	0.4 s, r=0.71	0.2 s, r=0.70	0.1 s, r=0.70

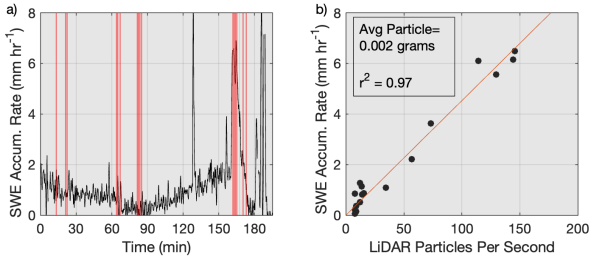

Figure 7: Time series of snowfall accumulation rates with LiDAR observations highlighted in red. Comparison of falling snow LiDAR particle counts immediately above snow scale against measured accumulation rates.

3.2. *Falling Snow Detection*

Figure 7 details snowfall accumulation rates during the four hours of simulated snowfall. Figure 7a shows a time series of the depth of water equivalent (SWE) accumulation rate (mm/hr) with LiDAR observation windows highlighted in red. As discussed below, the dendritic and aggregate grains in our snowfall experiment had a mean fall velocity around 1.5 m/s. For each LiDAR frame, we first counted the average number of grains in a 1.5 meter tall sub-volume inside our measurement domain immediately above the snow scale (blue box, Figure 2). This represents counting the number of particle returns in a region that likely accumulate on the snow scale in the following second. We expect the LiDAR to under count the true number of grains falling on the snow scale from six meters away, but these particle counts still provided us with a physically meaningful proxy for snowfall accumulation on the ground below. Spanning the seventeen experiments, Figure 7b shows a strong linear relationship between LiDAR backscatter and accumulation for snowfall rates spanning light (<1 mm SWE hr^{-1}), moderate (1 mm SWE hr^{-1} - 2.5 mm SWE hr^{-1}), and heavy (>2.5 mm SWE hr^{-1}) conditions, as classified by the Society of Automotive Engineers International Ground Deicing Committee and NCAR (Rasmussen et al., 2001). In Figure 7b we also plot the best linear fit with an enforced intersection at the origin (r^2 = 0.97). Even when the snowfall simulator was cleaning itself and generating extreme accumulation not typical in nature (>5 mm hr^{-1}), we find the correlation between LiDAR and snow scale data persists.

By forcing our linear relationship to intersect the origin, the slope of the line provides a best-fit average mass estimate for each snow particle return. This amounts to approximately 0.002 grams per LiDAR return. The LiDAR grid spacing was approximately 5 mm at 6 meters away. Very large aggregates created in the snowfall generator are discussed below, so we can approximate that each LiDAR return represents a voxel of snow no larger than 7 mm in diameter. As such, 0.002 grams is a large enough mass that we are likely undercounting the total number of accumulating particles, though this voxel mass is in line with some estimates of particles larger than 1 mm in diameter (e.g., Rees et al., 2021). Regardless, the strong linear relationship between the LiDAR and snow scale suggests the LiDAR particle count efficacy is consistent across slight, moderate, and heavy rates of snowfall. Due to the strong linearity of this relationship, and high r^2, only a few sixty-second measurements across these ranges are needed to obtain the conversion factor between LiDAR counts and true snowfall rates for this particle size and mass distribution. This indicates great promise for meaningful sub-second spatially resolved frozen hydrometeor measurements with 1550 nm LiDAR after determining the correct count-to-mass conversion factor.

When zooming back out and considering the full 144 m^3 measurement volume (orange dashed lines, Figure 2), a similarly strong correlation between total particle counts and snow accumulation rate exists (r^2 = 0.92) due to the relatively homogeneous nature of snowfall in the Cryospheric Environment Simulator, and the LiDAR's broad particle detection capabilities. A recreation of Figure 7 for the full measurement volume can be found in the Supplementary Material. When studying particles in the larger measurement volume, we find there is also a surprising opportunity to track large particles from one frame to the next.

Figure 8a shows one example frame of snowfall returns colored by their $\overline{NN}_{10}$ values. The angular scan pattern of the LiDAR generates a natural nonuniform distribution of $\overline{NN}_{10}$ values, with smaller values in the high-resolution inner region of interest. The distribution of $\overline{NN}_{10}$ in our snowfall scans, however, shows an anomalous dual-peak distribution (Fig. 8b) with many $\overline{NN}_{10}$ < 10 mm. These values are below inter-particle distances and correspond with multiple returns from individual large aggregate grains (e.g., Fig. 3). They also visible as bright spots in Figure 8a. Filtering our data to include only LiDAR returns with the lowest 10 percent of $\overline{NN}_{10}$ neighbor spacing, we find many large particle clusters that are easily tracked through multiple frames.

To track the falling snow and obtain particle velocities, we employ a simple centroid tracking algorithm. Given the LiDAR automatically provides (x, y, z) coordinates of these clusters (in contrast to traditional PTV), and the inter-particle spacing is much greater than intra-particle spacing, centroids for these clusters are easily obtained with automated density-based clustering algorithms (e.g., DBSCAN). This clustering and centroid calculation is equally helpful for obtaining accurate counts of individual grains where multiple returns on a single grain could skew snowfall rate statistics. The large separation between distinct centroids, the high frame-rate, and relatively slow speed of descent, makes matching particles from one frame to the next a relatively simple automated task. Our MATLAB particle tracking algorithm is included in the Supplementary Material. The algorithm outline is described in

the "Particle Tracking Algorithm" box.

Particle Tracking Algorithm

1. Extract all (x,y,z) lidar returns belonging to a frame.
2. Apply DBSCAN clustering to identify individual particles.
3. Compute the centroid of each cluster.
4. Initialize trajectories in the first frame.
5. Match centroids between consecutive frames using nearest-neighbor association.
6. Reject matches with positive vertical displacement.
7. Assign matched centroids to existing trajectories.
8. Create new trajectories for unmatched centroids.
9. Output trajectory tracks and labels

A sub-sample of particle tracks spanning the Figure 8a experiment are shown in Figure 8c. Tracks have been colored by their instantaneous vertical velocity. These particle trajectories are most easily tracked in the high-resolution inner sub-volume of the entire snowfall measurement domain (orange solid box, Figure 2). A small indoor fan blowing at approximately 1 m/s from outside the sampling measurement volume caused a slight drift of the particles, evident as migration of particles to the left of the frame in Figure 8c.

As validation of our large particle tracking, we calculated the distribution of instantaneous vertical velocities of these grains over all snowfall experiments. For each tracked cluster, we estimated its volume from the spatial extent of the clustered LiDAR returns and converted this volume to an equivalent spherical radius. This effective radius should not be interpreted as the $\overline{NN}_{10}$ spacing shown in Figure 8. Rather, it characterizes the size of the entire aggregate identified by the clustering procedure. Figure 9 compares the resulting distributions of aggregate size and fall velocity. The observed fall speeds are centered near 1.5 ms^{-1}, which is consistent with previous measurements of dendritic and aggregate snowflakes of comparable size under low-wind conditions (Ishizaka et al., 2016). The agreement between the inferred aggregate sizes and fall velocities provides additional confidence that the tracked clusters represent physically realistic snow particles rather than artifacts of the tracking algorithm.

4. Discussion

Through multiple laboratory experiments at the Cryospheric Environment Simulator, we find that the commercially available automotive-grade Seyond Falcon K1 1550 nm LiDAR is capable of meaningful spatial and temporal measurements of both blowing and falling snow. These two natural processes require the LiDAR to obtain accurate snow measurements under very different conditions. Raw data from the experiments

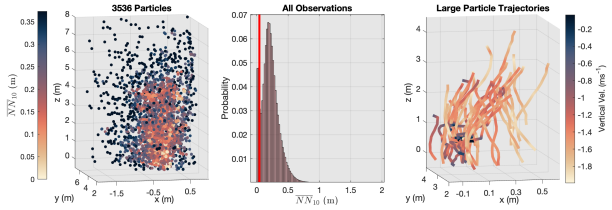

Figure 8: a) A single frame of laboratory falling snow detections colored by distance to neighbors in the larger $3m \times 6m \times 8m$ volume. b) Statistics of median neighbor distances showing spike in lowest 10th percentile indicating multiple returns on a single particle. c) Forty example trajectories of large particle centroids in the inner $0.7m \times 2m \times 4m$ high-resolution domain. Trajectories coincide with 60-seconds surrounding the panel a) frame, colored by fall speed.

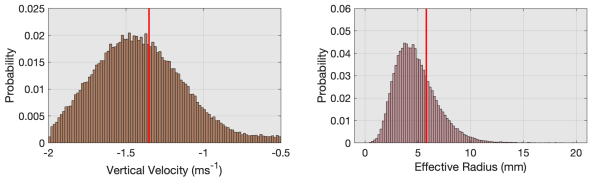

Figure 9: Probability distributions of particle fall speeds and effective radii for the largest "Type A" particle clusters that were able to be tracked in the snowfall experiments. Mean values are marked with a vertical red line.

generating Figures 6 and 8 can be found in the dataset published by Aksamit (2026).

During blowing snow, LiDAR surface snow transport measurements rely on an integrated volume backscatter that depends not only on the scattering efficiency of the individual particles, but also on particle size distributions and number concentrations. More than half of the saltating particles detected by the SPC in the wind tunnel experiments were smaller than 100 μm in diameter. Under these conditions, we find that the 1550 nm LiDAR's power is still sufficient to provide millimeter scale spatially resolved measurements of saltation clouds at 10 FPS.

The total number of LiDAR returns above 3 cm was nearly linearly related to SPC mass-flux measurements, suggesting that LiDAR particle counts provide a meaningful proxy for vertically integrated saltation flux. We find the LiDAR can also resolve spatially and temporally coherent saltation cloud structures with complex morphologies. Such features appear as peaks in SPC saltation flux and could be tracked through the wind tunnel in the LiDAR data with advection speeds in accordance with expected blowing snow velocities. For this reason, fast-scanning high-resolution LiDARs pose a significant advantage to spatially resolve snow transport phenomena.

For small blowing snow particles, Warren (2019) suggests 1550 nm is more sensitive to smaller ice particles with reflectance greater than the the often quoted <10% values. Additionally, we have reduced solar background radiance and increased absorption of ice at this wavelength. These aspects may also help improve the signal-to-noise ratio and reduce multiple scatterings, thus improving contrast and preserving spatial structures in dense blowing snow layers.

Our falling snow experiments provided a markedly distinct

scenario to test the 1550 nm LiDAR when compared with the blowing snow experiments. Dendritic and aggregate grains occurred in much sparser volumetric concentrations, and with much larger diameters than during the blowing snow tests. Additionally, variations between blowing snow and fresh snow microstructures may result in different refraction and reflection behaviors. Under these conditions the 1550 nm LiDAR particle counts were still found to be strongly linearly related to concurrent snowfall rates. This relationship spanned light, moderate, and extremely heavy snowfall. This suggests the LiDAR measurements were far from saturated and natural outdoor snowfall conditions are likely well within the LiDAR's operational capacity. Additionally, we were able to track large aggregate grains from one frame to the next, obtaining individual time varying particle velocities. Our particle tracking algorithm relies on a nearest-neighbor association and does not explicitly account for particle acceleration or temporary particle disappearance between scan lines. As such, tracking performance depends on the frame rate, particle size, and particle concentrations remaining sufficiently low to avoid ambiguous associations. This LiDAR-based approach, however, provides an entirely new method with which to measure snow particle velocities, and a relatively simple complement to traditional particle tracking velocimetry (e.g, Toloui et al., 2014; Aksamit and Pomeroy, 2016).

While the blowing and falling snow particles measured in this experiment were artificially generated in the Cryospheric Environment Simulator (Abe and Kosugi, 2019), we believe comparable measurements are possible in outdoor natural conditions for multiple reasons. The size range and distribution of the "Type B" blowing snow particles (Figure 4) were comparable to natural conditions. The sieved surface snow lacked the inter-particle cohesive forces found in natural snowpacks (e.g., Schmidt, 1982), and this lack of cohesion makes particles readily available for saltation. Saltation cloud densities in the wind tunnel, however, are representative of new snow equilibrium transport conditions and should be representative of the reflectivity of outdoor blowing snow clouds except for over particularly wind-hardened snowpacks. The particle morphologies of the dendrites and large aggregates in our snowfall experiments mimicked natural snow in calm winds, but their density is relatively low for natural conditions (20 kg/m^3, (Abe and Kosugi, 2019)). Higher particle densities would indeed facilitate greater reflectance and improve the falling particle counts in nature. The largest aggregates reached sizes not commonly found outdoors (e.g., Figure 3). These large particles were easily tracked as they appeared in multiple scan lines at distances up to ten meters away. Natural snowfall should be expected to be smaller in diameter, but such particle tracking may remain possible at closer distances. Lastly, while no outdoor measurements were detailed in this initial study, we have performed multiple natural snow tests and have had great preliminary success measuring outdoor blowing and falling snow in a variety of winter and spring Arctic conditions.

5. Conclusions and Future Work

The ability of a commercially available fast-scanning 1550 nm LiDAR to obtain meaningful measurements of snow particles spanning several orders of magnitude in diameter is a surprising finding. We show that the reduced reflectance of snow at this wavelength (e.g., Deems et al., 2013) does not preclude it from being a viable collection avenue of blowing and falling snow measurements. Instead, the ability to transmit higher power eye-safe signals with several orders of magnitude more photon density likely compensates for the roughly 8-9× lower reflectance. Indeed, we found promising measurement capabilities at distances much shorter than the advertised maximum range. Our usable detection range easily reached 10 meters, which would not be a limiting factor for site specific blowing and falling snow measurements or research campaigns.

Future field deployments of fast-scanning LiDAR are possible in many orientations, each with distinct advantages for blowing or falling snow studies. A ground-parallel orientation could provide helpful insight into vertical particle density profiles of blowing snow flux, as well as turbulence influences on falling snow organization. In such an orientation, effort may be needed to prevent a near-surface unit from becoming buried during blowing snow and to maintain a parallel view to the snow surface. Additionally, fast-scanning LiDAR units often have a minimum measurement distance on the order of several meters. Surface-parallel blowing snow measurements during very intense transport may prove difficult because of shadowing caused by particles closer than this minimum distance.

A complementary downward facing view, such as from a tall mast or UAV could provide new insight into the horizontal heterogeneity of blowing snow transport and improve our current understanding (e.g., Aksamit and Pomeroy, 2017; Nishimura et al., 2024). The passage of transport clouds should be readily identifiable as snow surface height anomalies, and a downward orientation would facilitate greater uniformity in scan line pattern spacing. Obvious limitations may arise depending on the height and stability of the UAV or mast as scan line patterns will become sparser at greater distances and oblique angles.

The ability to detect blowing and falling snow with 1550 nm LiDAR is likely not restricted to our specific manufacturer or model. Many manufacturers rely on the 1550 nm wavelength for "long-range" detection, which is directly correlated with the higher laser power we have benefited from in our study. Indeed, in a study focused on filtering airborne snow interference for autonomous driving applications, Mattson et al. (2025) found that an alternative automotive 1550 nm LiDAR consistently saw more airborne snow than a comparable automotive 905 nm LiDAR. Given the robust construction of these units, being designed to operate in cold, wet, and windy conditions for automotive applications, our experimental results suggest great potential for repurposing long-range fast-scanning automotive-grade LiDARs for further hydrological, meteorological and cryospheric studies. Future work should focus on calibration strategies linking optical

backscatter to particle size distributions and transport rates, as well as field validation under natural blowing snow conditions. Different scaling relationships (e.g., Figs. 4b and 7b) will need to be determined to relate LiDAR particle counts per volume to mass flux and accumulation rates with different precipitation types for given LiDAR configurations. A broader ability to measure particles will depend on the distance of interest from the unit, particle size distributions, and moisture content. Due to the strong linear relationship of LiDAR counts with blowing snow flux or snow fall rates across our wide range of experiments, determining the physical conversion factor will likely require only a few calibration experiments. This conversion factor would also likely be uniformly applicable for LiDARs with similar configurations.

Our experiments indicate we can collect rich time-resolved volumetric data of blowing and falling snow that is not possible with traditional single-point measurement tools such as snow traps, particle counters, or disdrometers. We believe future fast-scanning LiDAR studies may be able to address spatial hetereogeneities and intermittency in wind-snow coupling that has not yet been possible. The adoption of fast-scanning 1550 nm LiDAR in cryospheric studies may be a transformative tool studying turbulent transport, drift formation, and the role of coherent structures in organizing near-surface snow processes.

Acknowledgements

We wish to express our gratitude to Kazuma Togashi, Genzo Okawa, and Koichi Suzuki, members of the Cryospheric Environment Simulator staff, for their assistance with the experiment. We also wish to thank Jeremy Bos and Alexander Prokop for illuminating conversations about LiDAR performance. Figures were generated using the *Scientific colour maps* from Fabio Crameri: https://doi.org/10.5281/zenodo.1243862. This research was funded in part by UiT's High Score and PES programs. Raw data used to generate Figures 6 and 8 are available in (Aksamit, 2026)

References

Abe, O., Kosugi, K., 2019. Twenty-year operation of the Cryospheric Environment Simulator. Bulletin of Glaciological Research 37, 53–65. doi:10.5331/bgr.16SR01.

Aksamit, N., 2026. Measurement and tracking of blowing and falling snow particles using an automotive 1550 nm lidar: Example raw data. URL: https://doi.org/10.5281/zenodo.2083961, doi:10.5281/zenodo.2083961.

Aksamit, N.O., Pomeroy, J.W., 2016. Near-surface snow particle dynamics from particle tracking velocimetry and turbulence measurements during alpine blowing snow storms. The Cryosphere 10, 3043–3062. doi:10.5194/tc-10-3043-2016.

Aksamit, N.O., Pomeroy, J.W., 2017. The Effect of Coherent Structures in the Atmospheric Surface Layer on Blowing-Snow Transport. Boundary-Layer Meteorology 167, 1–23. doi:10.1007/s10546-017-0318-2.

Clemens-sewall, D., Parno, M., Perovich, D., Polashenski, C., Raphael, I.A., 2022. FlakeOut : A geometric approach to remove wind-blown snow from terrestrial laser scans. Cold Regions Science and Technology 201, 103611. URL: https://doi.org/10.1016/j.coldregions.2022.103611, doi:10.1016/j.coldregions.2022.103611.

Dai, Z., Li, Y., Sundermeier, M.C., Grabe, T., Lachmayer, R., 2021. Lidars for vehicles : from the requirements to the technical evaluation, in: 9th International Forum on Automotive Lighting (IFAL), Shanghai, China.

Deems, J.S., Painter, T.H., Finnegan, D.C., 2013. Lidar measurement of snow depth: A review. Journal of Glaciology 59, 467–479. doi:10.3189/2013JoG12J154.

Gossart, A., Souverijns, N., Gorodetskaya, I.V., Lhermitte, S., Lenaerts, J.T.M., Schween, J.H., Mangold, A., Laffineur, Q., van Lipzig, N.P.M., 2017. Blowing snow detection from ground-based ceilometers: application to East Antarctica. The Cryosphere , 1–25doi:10.5194/tc-2017-89.

Hahner, M., Sakaridis, C., Bijelic, M., Heide, F., Yu, F., Dai, D., Van Gool, L., 2022. LiDAR Snowfall Simulation for Robust 3D Object Detection. Proceedings of the IEEE Computer Society Conference on Computer Vision and Pattern Recognition 2022-June, 16343–16353. doi:10.1109/CVPR52688.2022.01588, arXiv:2203.15118.

Ishizaka, M., Motoyoshi, H., Yamaguchi, S., Nakai, S., Shiina, T., Muramoto, K.I., 2016. Relationships between snowfall density and solid hydrometeors, based on measured size and fall speed, for snowpack modeling applications. Cryosphere 10, 2831–2845. doi:10.5194/tc-10-2831-2016.

Jokela, M., Kutila, M., Pyykönen, P., 2019a. Testing and Validation of Automotive Point-Cloud Sensors in Adverse Weather Conditions. Applied Sciences 9. doi:doi:10.3390/app9112341.

Jokela, M., Pyykönen, P., Kutila, M., Kauvo, K., 2019b. LiDAR Performance Review in Arctic Conditions, in: 2019 IEEE 15th International Conference on Intelligent Computer Communication and Processing (ICCP), Cluj-Napoca, Romania. pp. 27–31. doi:doi:10.1109/ICCP48234.2019.8959554.

Kinar, N.J., Pomeroy, J., 2015. Measurement of the physical properties of the snowpack. Reviews of Geophysics 53. doi:10.1002/2015RG000481.Received.

Kutila, M., Pyykönen, P., Jokela, M., Gruber, T., Bijelic, M., Ritter, W., 2020. Benchmarking Automotive LiDAR Performance in Arctic Conditions, in: 2020

IEEE 23rd International Conference on Intelligent Transportation Systems (ITSC), Rhodes, Greece, pp. 1–8. doi:10.1109/ITSC45102.2020.9294367.

Li, C., Lim, K., Berk, T., Abraham, A., Heisel, M., Guala, M., Coletti, F., Hong, J., 2021. Settling and clustering of snow particles in atmospheric turbulence. Journal of Fluid Mechanics 912, 1–24. doi:10.1017/jfm.2020.1153, arXiv:2006.09502.

Li, J., Guala, M., Hong, J., 2024. Field investigation of 3D snow settling dynamics under weak atmospheric turbulence. Journal of Fluid Mechanics 997, A33. URL: http://arxiv.org/abs/2406.08737, doi:10.1017/jfm.2024.601, arXiv:2406.08737.

Löffler-Mang, M., Joss, J., 2000. An Optical Disdrometer for Measuring Size and Velocity of Hydrometeors. Journal of Atmospheric and Oceanic Technology 17, 130–139.

Mattson, I.Q., Schexnaydre, L., Bos, J.P., 2025. Red versus Infrared: comparing 900nm and 1550nm Lidar performance in arctic winter conditions, in: Anguita, J.A., Wayne, D.T. (Eds.), Laser Communication and Propagation through the Atmosphere and Oceans XIV, International Society for Optics and Photonics. SPIE. p. 1361702. doi:10.1117/12.3064732.

Muller, K., 2025. Using experimental fluid dynamics to track natural snowfall. Nature Reviews Earth Environment , 43017URL: http://dx.doi.org/10.1038/s43017-025-00748-w, doi:10.1038/s43017-025-00748-w.

Nemoto, M., Sato, T., Kosugi, K., 2014. Effects of Snowfall on Drifting Snow and Wind Structure Near a Surface. Boundary-Layer Meteorology 152, 395–410. doi:10.1007/s10546-014-9924-4.

Nishimura, K., Nemoto, M., Ito, Y., Omiya, S., Shimoyama, K., Niiya, H., 2024. Elucidation of Spatiotemporal structures from high-resolution blowing snow observations. The Cryosphere 18, 4775–4786.

Palm, S.P., Kayetha, V., Yang, Y., Pauly, R., 2017. Blowing snow sublimation and transport over Antarctica from 11 years of CALIPSO observations. Cryosphere 11, 2555–2569. doi:10.5194/tc-11-2555-2017.

Prokop, A., 2008. Assessing the applicability of terrestrial laser scanning for spatial snow depth measurements. Cold Regions Science and Technology 54, 155–163. URL: http://dx.doi.org/10.1016/j.coldregions.2008.07.002, doi:10.1016/j.coldregions.2008.07.002.

Rasmussen, R., Dixon, M., Hage, F., Cole, J., Wade, C., Tuttle, J., Mcgettigan, S., Carty, T., Stevenson, L., Fellner, W., Knight, S., Karplus, E., Rehak, N., 2001. Weather Support to Deicing Decision Making (WSDDM): A Winter Weather Nowcasting System. Bulletin of the American Meteorological Society 82, 579–596.

Rees, K.N., Singh, D.K., Pardyjak, E.R., Garrett, T.J., 2021. Mass and density of individual frozen hydrometeors. Atmospheric Chemistry and Physics 21, 14235–14250. doi:10.5194/acp-21-14235-2021.

Ruttner, P., Voordendag, A., Hartmann, T., Glaus, J., Wieser, A., Bühler, Y., 2025. Monitoring snow depth variations in an avalanche release area using low-cost lidar and optical sensors. Natural Hazards and Earth System Sciences 25, 1315–1330.

Sato, T., Kimura, T., Ishimaru, T., Maruyama, T., 1993. Field test of a new snow-particle counter (SPC) system. Annals of Glaciology 18, 149–154. doi:10.3189/s0260305500011411.

Schmidt, R.A., 1982. Properties of blowing snow. Reviews of Geophysics 20, 39–44. doi:10.1029/RG020i001p00039.

Sun, C., Sun, P., Wang, J., Guo, Y., Zhao, X., 2024. Understanding LiDAR Performance for Autonomous Vehicles Under Snowfall Conditions. IEEE Transactions on Intelligent Transportation Systems 25, 16462–16472. doi:10.1109/TITS.2024.3409907.

Tapiador, F.J., Turk, F.J., Petersen, W., Hou, A.Y., García-ortega, E., Machado, L.A.T., Angelis, C.F., Salio, P., Kidd, C., Huffman, G.J., Castro, M.D., 2012. Global precipitation measurement : Methods , datasets and applications. Atmospheric Research 104-105, 70–97. URL: http://dx.doi.org/10.1016/j.atmosres.2011.10.021, doi:10.1016/j.atmosres.2011.10.021.

Teufel, S., Volk, G., Bernuth, A.V., Bringmann, O., 2022. Simulating Realistic Rain , Snow , and Fog Variations For Comprehensive Performance Characterization of LiDAR Perception, in: 2022 IEEE 95th Vehicular Technology Conference: (VTC2022-Spring), IEEE. pp. 1–7. doi:10.1109/VTC2022-Spring54318.2022.9860868.

Toloui, M., Riley, S., Hong, J., Howard, K., Chamorro, L.P., Guala, M., Tucker, J., 2014. Measurement of atmospheric boundary layer based on super-large-scale particle image velocimetry using natural snowfall. Experiments in Fluids 55, 14. URL: http://link.springer.com/10.1007/s00348-014-1737-1, doi:10.1007/s00348-014-1737-1.

Wang, W., You, X., Chen, L., Tian, J., Tang, F., Zhang, L., 2022. A Scalable and Accurate De-Snowing Algorithm for LiDAR Point Clouds in Winter. Remote Sensing 14, 1–23. doi:10.3390/rs14061468.

Warren, S.G., 2019. Optical properties of ice and snow. Philosophical Transactions of the Royal Society A: Mathematical, Physical and Engineering Sciences 377. doi:http://dx.doi.org/10.1098/rsta.2018.0161.

Wojtanowski, J., Zygmunt, M., Kaszczuk, M., Mierczyk, Z., Muzal, M., 2014. Comparison of 905 nm and 1550 nm semiconductor laser rangefinders' performance deterioration

due to adverse environmental conditions. Opto-Electronics Review 22, 13–20. doi:10.2478/s11772.